Pergamon

Atmospheric Environment Vol. 29, No. 16, pp. 2177–2189, 1995

1352-2310/95 $9.50 + 0.00

1352-2310(94)00237-1

ROLE OF MESOSCALE CIRCULATIONS ON MONSOON RAINFALL OVER THE WEST COAST OF INDIA

NEERAJA C. REDDY and SETHU RAMAN

Department of Marine Earth and Atmospheric Sciences, North Carolina State University, Raleigh, NC 27695-8208, U.S.A

(*First received* 18 *February* 1993 *and in final form* 1 *May* 1994)

Abstract—Sensitivity of monsoon rainfall to different ambient wind speeds, orography and wind shear was studied using a two-dimensional mesoscale model. Three numerical experiments were performed with different initial uniform ambient wind speeds ($U = 0.1\ m\ s^{-1}$, $5\ m\ s^{-1}$ and $10\ m\ s^{-1}$) for a typical summer day. It was found that the rainfall increased over the mountain slopes as the initial ambient wind increased. As expected, sheared flow produced increased amounts of precipitation as compared to the uniform ambient flow.

Effect of sea/land temperature difference on monsoon rainfall was also investigated. Incorporation of diurnal heating caused the surface pressure gradient to increase, leading to local accelerations of winds, increased mesoscale circulations and more rainfall. The model did not predict precipitation when the orography was not considered.

Key words index: Numerical model, monsoon rain, India,

1. INTRODUCTION

The important challenge in developing strategies for sustainable development is to predict the future states of climate. The Indian summer monsoon is a component of large scale circulation system. This monsoon occupies an area of about one-seventh of the entire earth surface. Circulations and associated weather patterns in the monsoon atmosphere are governed by a variety of complex interactions such as air–sea–land temperature gradients, orography, cumulus convection and cloud–radiation interaction.

Principal components of the large scale circulation system are the Hadley cell and the Walker circulations. The Hadley cell is a thermally driven circulation which transports heat towards the poles. In the Northern Hemispheric summer, the ascending branch of the Hadley cell moves northward, driven by the heating of the land masses. This ascending branch of the Hadley cell is commonly referred to as the Intra Tropical Convergence Zone (ITCZ). The surface convergence at the ITCZ is the driving mechanism for the summer monsoon circulation. The northward drift of the Hadley cell causes deep convection over the warm pool of water in the western tropical Pacific ocean, located at about 100 E. The latent heating in the deep convection drives another direct circulation, known as walker circulation/El Nino. Convective activity over the Indian peninsula interacts with Walker circulation, creating an upper level jet over south India around 13°N latitude. Monsoon circulation also has an effect on the Walker circulation. For example, intense heating over India causes upper level easterly jet to intensify which modifies the circulation over the tropical western Pacific. An active monsoon also causes stronger southerly flow across the equator into the Arabian Sea.

The west coast of India receives significant amounts of rainfall as a result of the southwest monsoon. Several processes are believed to contribute to the variations in the magnitudes and the distribution of the clouds and the rainfall: (1) orographic lifting of the air parcels by the Western Ghats (Sarka *et al.*, 1978), (2) diurnal heating over land causing temperature differences between land and sea producing mesoscale circulations along the coast, (3) convective instability over the Arabian Sea (Smith and Lin, 1983) partly induced by the local accelerations of the Somali jet, (4) moisture flux from the Arabian Sea (Alapaty *et al.*, 1993), and (5) presence of offshore vortices (Mukherjee *et al.*, 1981).

The Western Ghats parallel the coast about 100 km inland between 8.5° and 21°N latitude and have a mean altitude of 1000 m, though individual peaks are much higher. These mountains extend about 1600 km in the north–south direction. The land immediately along the coast receives considerable rainfall while the western slopes of the Ghats receive even more (Smith and Lin, 1983). Immediately beyond the crest of the mountains the rainfall rate decreases to a low value.

Southwest monsoon weather is characterized by the presence of strong low-level westerly flow. Boundary

layer processes over this region are complex due to the presence of the low-level Somali jet over the Arabian Sea and convective processes associated with the orographic lifting of moist air along the west coast of India. The core of the Somali jet is situated at an altitude between 1 and 2 km. Presence of this jet causes strong low-level wind shear.

Recently, Ogura and Yoshizaki (1988) used a two-dimensional compressible, moist cloud model to study the rainfall patterns over the Western Ghats region. They considered the effects of heat fluxes and a sheared environment. Their results show that orographically forced upstream lifting is stronger in a sheared flow as compared to a vertically uniform flow. However, Ogura and Yoshizaki (1988) did not study the possible effects of coastal mesoscale circulations.

The main objectives of this study are to investigate the roles of the Western Ghats, diurnal variation of land surface heating and the upstream wind shear on monsoon rainfall. For this purpose, a two-dimensional mesoscale model with higher-order turbulence closure and explicit cloud physics was used. A brief description of the physical components of the numerical model is given in Section 2. Experiment design and the initial and boundary conditions used in the model are described in Section 3 and the results from the numerical experiments are discussed in Section 4.

2. MODEL DESCRIPTION

The two-dimensional mesoscale numerical model used in this study is described by Huang and Raman (1991). The model is hydrostatic and anelastic in a terrain following coordinate system. The prognostic model includes horizontal momentum equations, thermodynamic equation for the potential temperature, and conservation equations for water vapor (q), cloud water (q_c) and rain water (q_r).

The atmospheric planetary boundary layer is treated separately as the surface layer and transition layer in the model. To account for the surface layer turbulent transport, the surface-layer similarity stability functions given by Businger *et al.* (1971) are used (see Huang, 1990). Above the surface layer, a turbulence closure scheme using the turbulent kinetic energy (TKE) and dissipation (ε) is incorporated with the level 2.5 scheme of Mellor and Yamada (1982) determining the eddy diffusivities in the transition layer.

Ground temperature is obtained from the surface energy balance equation, but sea surface temperatures are held constant. The radiation scheme used in this model incorporates long-wave and short-wave radiative transfer and is similar to the one used by Mahrer and Pielke (1977). This scheme takes into account the absorption of short-wave radiation by water vapor and long-wave energy emitted by water vapor and carbon dioxide. A modified Warming–Kutler–Lomax (WKL) advection scheme (Huang and Raman, 1992) is used in the horizontal and a quadratic upstream interpolation in the vertical. Potential temperature, U and V components of mean wind, and relative humidity profiles are specified at the initial time. The initial profiles of these variables represent a typical monsoon sounding over the Arabian sea obtained from FGGE level IIIb data (Fig. 1). Initial conditions are obtained using an Ekman-layer type balance equation. The relative humidity on the ground is held constant. At the upper boundary, radiation boundary condition (Klemp and Durran, 1983) is used to determine the upper perturbation pressure. A prognostic scheme (Miller and Thorpe, 1981) is applied to the lateral inflow boundary grids, while the prediction equations are used at the lateral outflow boundary grids.

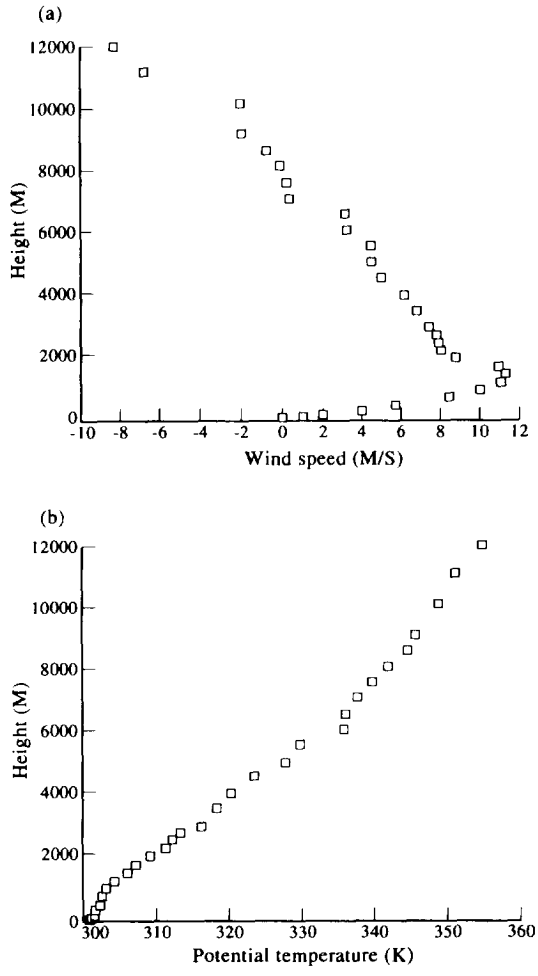

Fig. 1. Typical monsoon sounding obtained from FGGE level IIIb (a) wind speed profile and (b) potential temperature profile.

3. EXPERIMENT DESIGN

The primary objective is to examine the influence of the ambient wind, orography, diurnal variations and upstream wind shear on the monsoon rainfall along the west coast of

Table 1. Numerical experiments

Case	Winds	Mountain	Energy balance
C1	0.1	Yes	Yes
C2	5	Yes	Yes
C3	10	Yes	Yes
C4	5	No	Yes
C5	10	Yes	No
C6	Shear (A typical monsoon sounding Fig. 1a)	Yes	Yes

India. For this purpose, six numerical sensitivity studies were conducted for a typical summer day with the assumption that neither tropical nor frontal systems are present for the period of simulation. Description of the numerical experiments is given in Table 1.

A two-dimensional version of the mesoscale numerical model described in Section 2 is used. The 3-D version of this model could provide a better dynamical understanding, particularly regarding the Somali jet features. However, since the Western Ghats are parallel to and cover most of the western coast of India, assumption of two dimensionality of the flow is reasonable for the objectives of this study.

Numerical experiments for cases C1, C2 and C3 were conducted to examine the influence of the variation in the ambient wind speeds. Uniform southwesterly ambient winds were used for this purpose. Case C4 was conducted to examine the role of the Western Ghat mountains on monsoon rainfall. Differential heating and surface roughness between land and water are important factors in causing mesoscale convergence. The relative importance of differential surface heating on the mesoscale circulation was examined in case C5. Case C6 investigated the importance of wind shear on monsoon rainfall. For this purpose, a typical monsoon sounding (Fig. 1a) was used.

Other prescribed parameters and large scale variables used in the model were identical for all cases. The model domain contained 30 vertical layers to cover a height of 12 km. The horizontal domain included 240 east–west grids with a uniform grid interval of 5 km. Coastline is at grid 97, with ocean to the west. A constant sea surface temperature of 25°C was used over the ocean and a constant ground temperature of 35°C is used over land as initial condition. Relative humidity was assumed to be 90% below the depth of monsoon circulation (4 km) and then decreasing linearly above. A typical monsoon sounding for potential temperature (θ) obtained from FGGE level IIIb data was used (Fig. 1b). The model was integrated for one diurnal cycle (24 h) to include the sea/land breeze heating cycle with an integration time interval of 10 s. Figure 2a shows the surface elevation of the Indian subcontinent. Flat area indicates the ocean. The Western Ghats are along the west coast of India and Himalayan mountains are to the north. The solid line indicates the two-dimensional model domain used for this study located at 13°N. Figure 1b shows the topography at 13°N used for the simulations. The 10 min topography data shown in Fig. 2b were obtained from the U.S. Navy. A roughness length of 10 cm was assumed over land, while Charnock's relationship was used over water. The arrow along x-axis of Fig. 2b indicates the coastline.

4. DISCUSSION AND RESULTS

In this section, numerical model results obtained from different sensitivity tests are discussed. Again, the objectives were to isolate the effects of the orography, diurnal variations and upstream wind shear. Figure 3 shows the ground temperatures as computed from the surface energy budget at different model hours for Case C2. Though a 10°C temperature difference between land and sea are given initially (zero hour), the model takes six hours to spin up, to adjust to the prescribed temperatures as can be seen in Fig. 3.

4.1. *Uniform winds*

(a) *With mountains.* Three numerical experiments were conducted with different uniform ambient winds: (1) 0.1 m s^{-1}, (2) 5 m s^{-1} and (3) 10 m s^{-1}. In each of these experiments, the model included an energy budget that accounts for diurnal variation of land surface processes. The land–sea temperature difference induces surface heat flux gradients which in turn causes local pressure gradients driving mesoscale circulations.

For case C1 (initial $U = 0.1$ m s^{-1}), by the third hour of model simulation (0700 LST), a horizontal potential temperature gradient and a horizontal pressure gradient begin to form as a result of the heating of the land (not shown). The distributions of U and W (vertical velocity) at 6 h (1000 LST) indicate a wave structure and an upwind phase tilting (Fig. 4a). a strong updraft is formed over the upwind slope of the mountain. A low-level jet begins to form near the coastline with a maximum speed of 4.2 m s^{-1} due to the sea breeze circulation. Thus the winds have accelerated from 0.1 to 4.2 m s^{-1} in 6 h because of the convergence (1.2×10^{-4} s^{-1}) over the coastal area (100 km) associated with the sea breeze circulation which extended to a depth of about 1.5 km. The dashed lines in Fig. 4a and b show the potential temperature (θ) after 6 h of integration (1000 LST). A convective boundary layer developed by 1000 LST over land. As can be seen from Fig. 3, ground temperatures reached a maximum at model hour 6 and remained approximately constant until hour 9 (1300 LST). The thermodynamic structure shows a strong development of the boundary layer near the land–sea interface. The convective boundary layer reached a maximum height of 1.5 km upwind of the mountains near the coast. Cloud water distribution after six hours of integration is shown in Fig. 4b. Convective clouds (Fig. 4b) formed over the mountain peak and over the upwind slope of the mountain to a height of about 2 km. However, the model did not predict any rain water at 6 h (not shown).

Depth of the sea breeze circulation increased to 2 km by 12 h (1600 LST, not shown). Low level winds increased to 10.7 m s^{-1} by this hour (not shown). A maximum vertical velocity of 35 cm s^{-1} was predicted over the mountain slope, with weak upward velocities of 4 cm s^{-1} at the coastline (not shown). A maximum in cloud water of 0.46 g kg^{-1} was simulated over the mountain slopes, but no cloud water was evident upwind. Ascending motions were weak at the coastline ($W = 4$ cm s^{-1}). Still no rain water occurred.

(a)

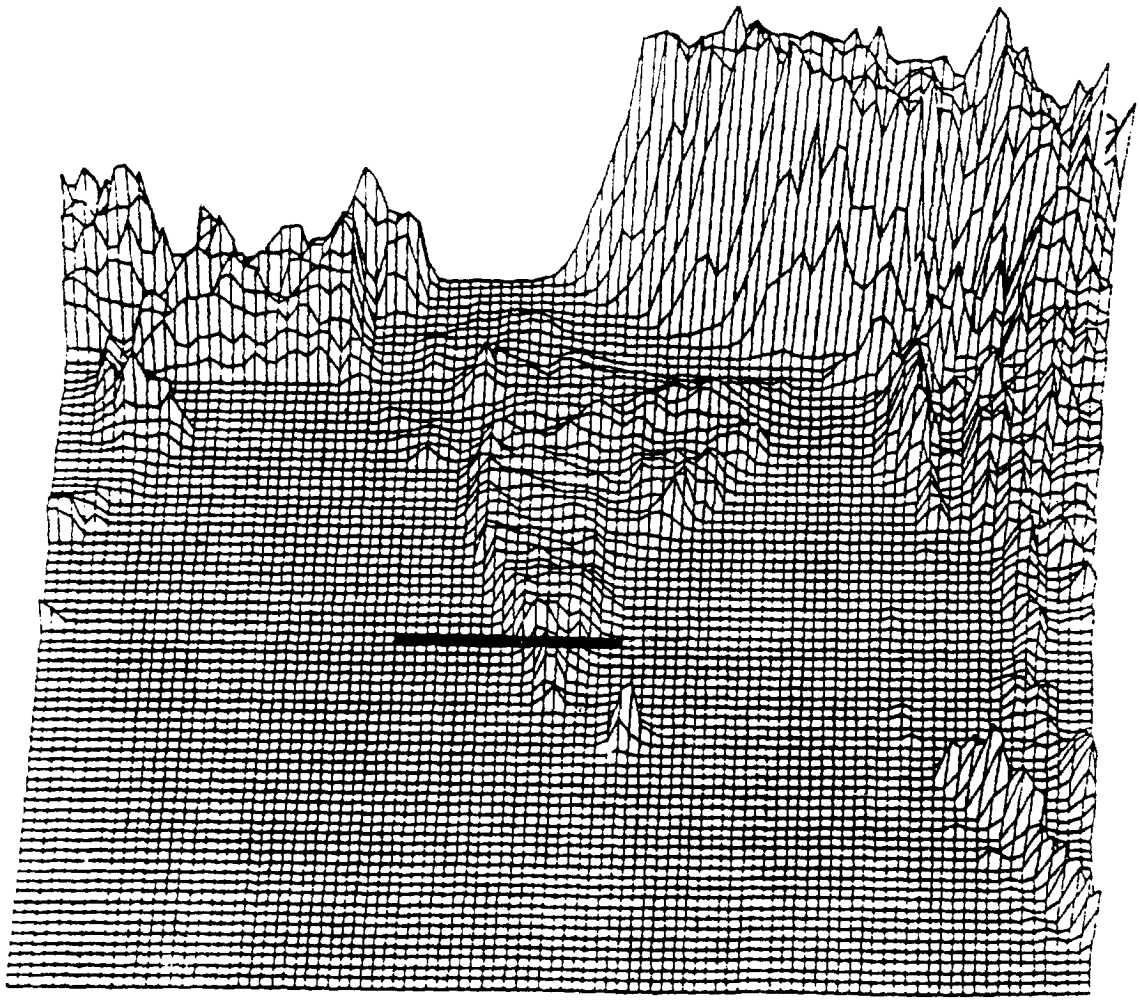

(b)

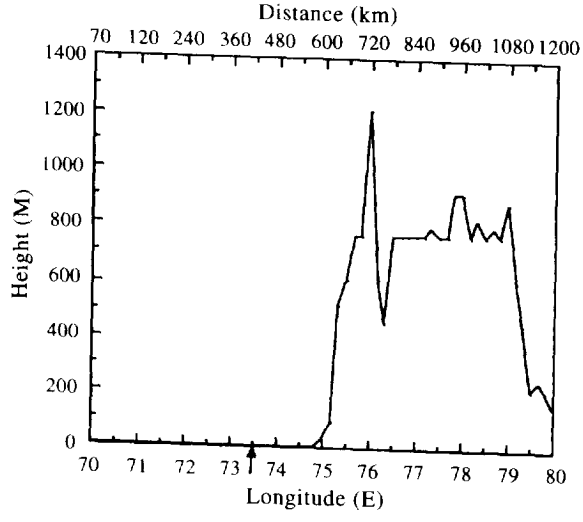

Fig. 2. (a) Surface elevation of the simulated region. Flat area indicates the ocean. The bold line indicates the model domain in the horizontal for the 2-D model. (b) 10′ Navy topographical data used in the model. The arrow on x-axis indicates the coastline.

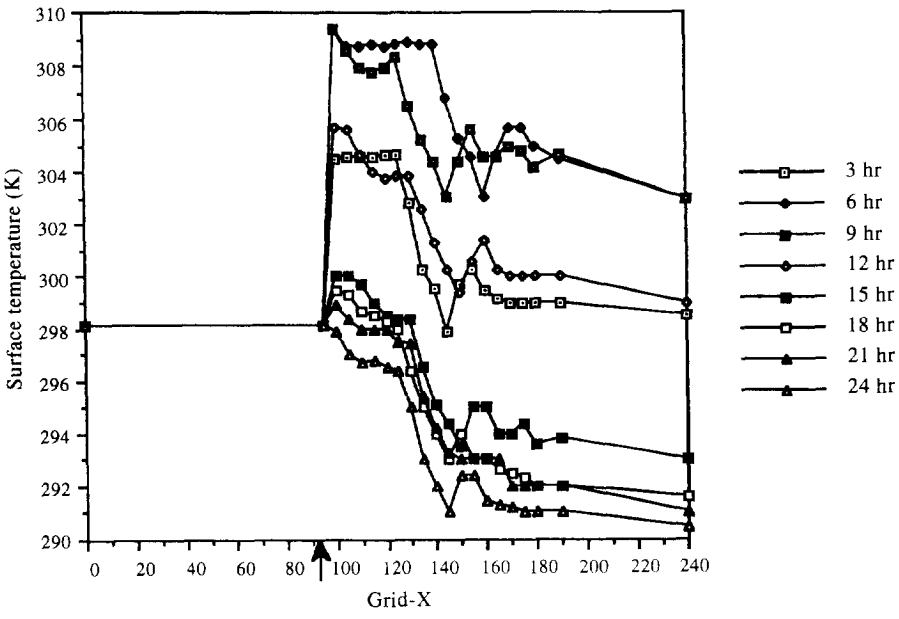

Fig. 3. Ground temperatures obtained from Case C2 at different model hours. The horizontal line indicates the constant sea surface temperatures.

Figure 5 shows the distributions of cloud water and rain water after 15 h of model integration (1900 LST). Cloud height over the mountains increased to 3 km (Fig. 5a) as compared to 2 km at 12 h (1600 LST). Distribution of rainfall is shown in Fig. 5b. Maximum rainfall of 0.8 mm h^{-1} was predicted over the mountain peak. Precipitation was also predicted over the upwind mountain slopes. Maximum rain rate of 5.0 mm h^{-1} is predicted over the mountain slopes at 21 h (0100 LST). However, no rainfall was predicted over the coastline and offshore. A land breeze circulation obviously did not develop. As can be seen from Fig. 3, the land–sea temperature difference over the coastal region (100 km) during nighttime was only about 1–2°C whereas during day time, a temperature difference of 8–10°C occurred, inducing strong sea breeze circulation.

In case C2, the ambient wind was assumed to be 5 m s^{-1} in order to investigate the effect of moderate winds on mesoscale circulations. A comparison of the U and the W fields at 6 h with those of case C1 (weak ambient wind) indicates a similar wave structure upwind of the mountains. The upstream tilting mountain waves, however, are much stronger in case C2. The maximum vertical velocity (20 cm s^{-1}) and cloud water (0.3 g kg^{-1}) have increased by a factor of two in case C2 as compared to case C1. Predicted boundary layer height was about 1800 m, an increase of 300 m over the case C1. At 12 h, the depth of sea breeze circulation increased to 2.5 km as compared to 2 km for C1 possibly due to stronger winds producing larger surface fluxes over water. A mesoscale convergence of $2.3 \times 10^{-4}\,s^{-1}$ is estimated for case C2 as compared to $1.5 \times 10^{-4}\,s^{-1}$ for C1 at model hour 12 near the coast (100 km). Cumulus clouds extended to a height of about 4 km. Also, rain water (0.4 mm h^{-1}) was predicted at this hour, as opposed to no rainfall for C1. Rainfall occurred only after 15 h of model simulation for case C1.

Distributions of U, θ, q_c and q_r after 15 h (1900 LST) of model simulation are shown in Fig. 6. The U-field is quite similar to case C1. The planetary boundary layer over land has become stable due to nocturnal cooling. Maximum vertical velocity again occurred over the mountains with a magnitude of 70 cm s^{-1}. This value is about 15% higher as compared to case C1 where a maximum vertical velocity of 60 cm s^{-1} was predicted. Cloud water (q_c) formed over a broader region and extended to higher levels (3 km) as compared to the case C1. Maximum value of cloud water increased to 0.6 g kg^{-1}. This is believed to be due to the increased mesoscale convergence ($3.0 \times 10^{-4}\,s^{-1}$). Increased cloud water content led to increased rainfall. A maximum rainfall rate of 2.4 mm h^{-1} was predicted (Fig. 6c), an increase by a factor of three as compared to case C1.

During the southwest monsoon, surface winds are generally of the order of 10 m s^{-1} and higher (Grossman and Durran, 1984). In case 3 (C3), an ambient wind of 10 m s^{-1} was used. Mean structure of the U and W fields was essentially the same for this case as that predicted for cases C1 and C2, except for increased turbulent mixing in the boundary layer due to increased winds. In all the three simulations, clouds developed first near the mountain peak, being the area of maximum orographically induced ascent. Figure 7 shows the distributions of U and θ and cloud and rain water after 6 h (1000 LST) of model integration.

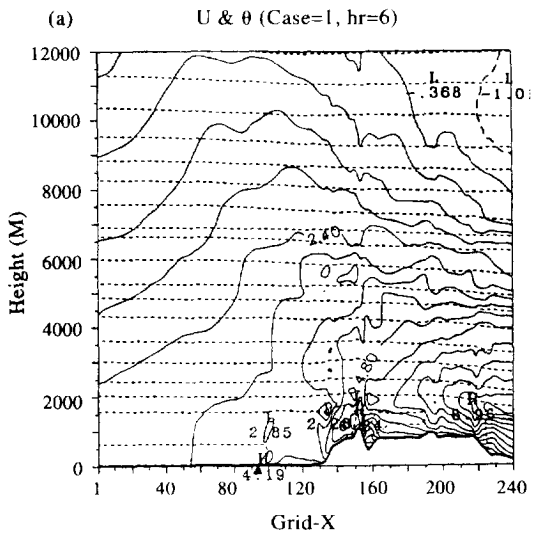

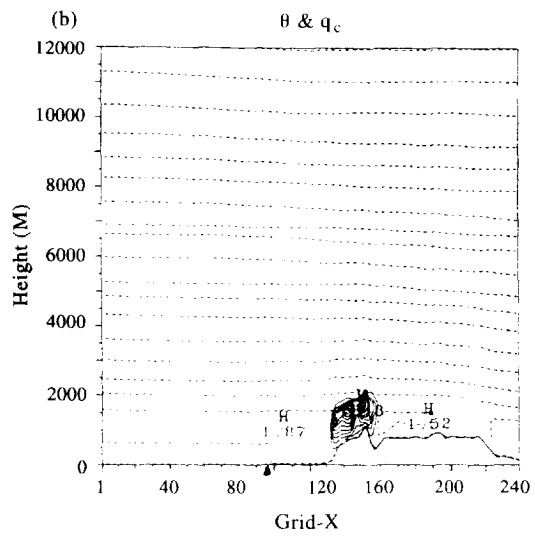

Fig. 4. Predicted (a) U and θ fields and (b) θ and cloud water, q_c at 6 h for Case C1. The minimum, maximum and contour interval for U-field are $-0.6\ m\ s^{-1}$, $8.4\ m\ s^{-1}$ and $0.6\ m\ s^{-1}$ respectively. The minimum, maximum and contour interval for θ-field are 297, 360 and 3 K, respectively. The minimum, maximum and contour interval for cloud water (q_c) are 0, 0.18 and 0.01 g kg^{-1}, respectively. Dashed lines indicate the θ surfaces. The coastline is indicated by a triangle on x-axis.

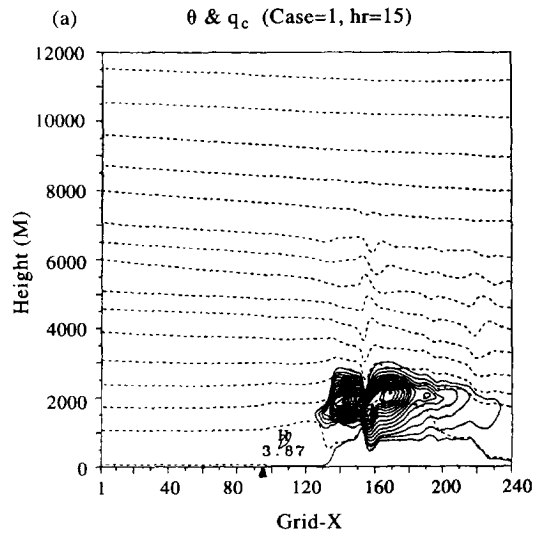

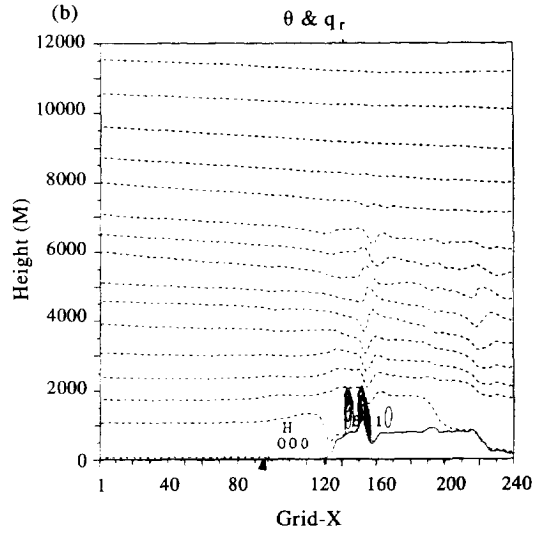

Fig. 5. Predicted (a) θ and cloud water, q_c and (b) θ and rain water, q_r at 15 h for Case C1. The minimum, maximum and contour interval for θ-field are 296, 364 and 4 K respectively. The minimum, maximum and contour interval for cloud water (q_c) are 0, 0.54 and 0.03 g kg^{-1}, respectively. The minimum maximum and contour interval for rain water (q_r) are 0, 0.8 and 0.05 mm h^{-1}, respectively. Dashed lines indicate the θ surfaces. The coastline is indicated by a triangle on x-axis.

In this early stage (6 h), distributions of clouds in Case 3 were broader and more intense as compared to C2. The maximum cloud water occurred over the upwind mountain slopes, with a maximum value of 0.6 g kg^{-1} (Fig. 7b) which is approximately twice that for case C2 and four times that for case C1 (Fig. 5). The U-field (Fig. 7a) showed a similar wave structure as in cases C1 and C2; however, the upstream tilting mountain waves were much stronger compared to cases C1 and C2. Three strong cells formed over the mountains and the upwind slopes, with a maximum surface precipitation of 3.2 mm h^{-1} (Fig. 7c). Maximum vertical velocities at 1000 LST (model hour 6) increased by a factor of three to 60 cm s^{-1} as compared to lower ambient wind cases.

The most significant differences between these three experiments become increasingly evident with time. In Case 3, stratiform clouds formed over the ocean at

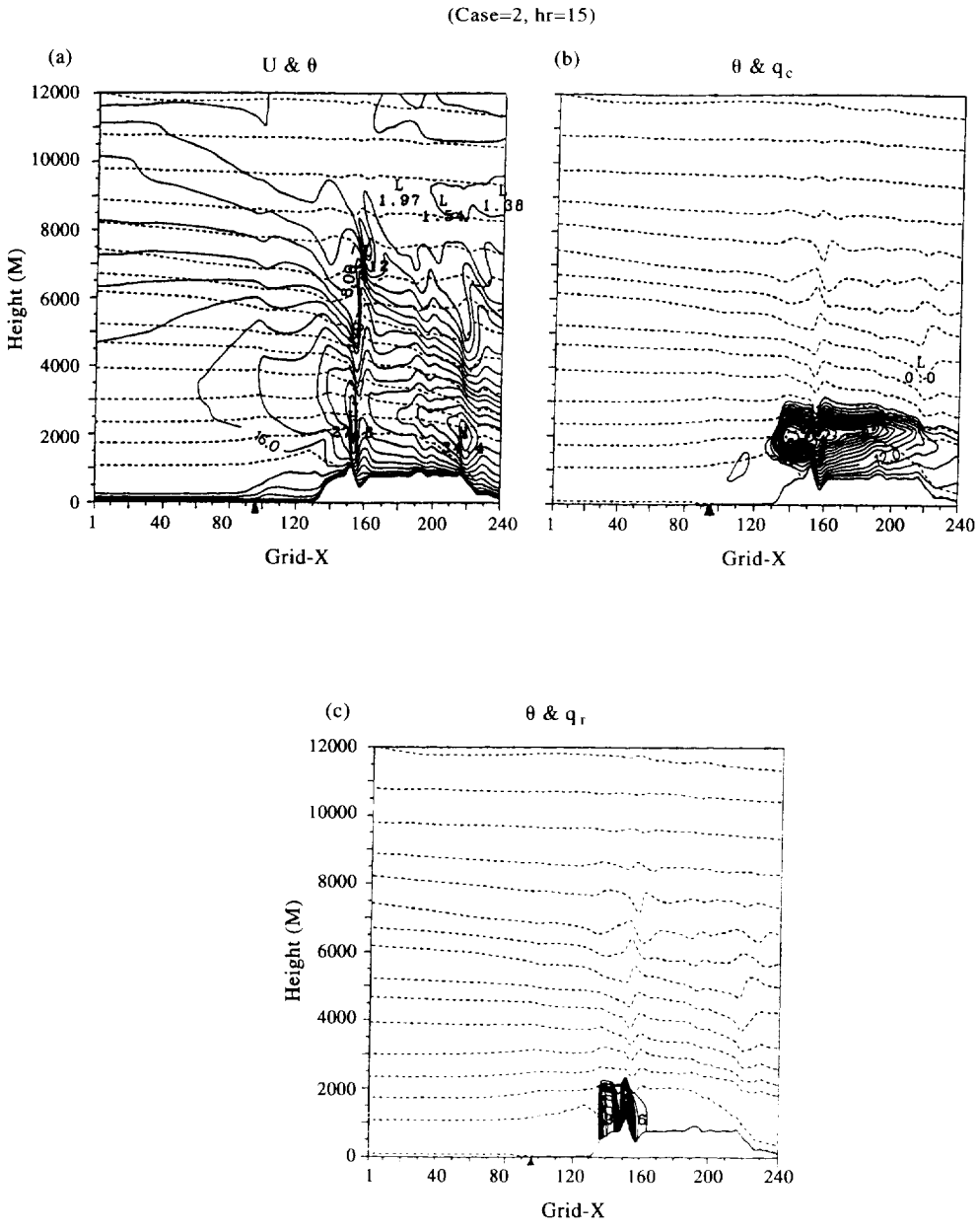

Fig. 6. Predicted (a) U and θ fields, (b) θ and cloud water, q_c (c) θ and rain water, q_r at 15 h of model simulation for Case C2. The minimum, maximum and contour interval for U-field are 0, 26 and 1.0 m s^{-1}, respectively. The minimum, maximum and contour interval for θ–field are 297, 364 and 4 K, respectively. The minimum, maximum and contour interval for cloud water (q_c) are 0, 0.6 and 0.03 g kg^{-1}, respectively. The minimum, maximum and contour interval for rain water (q_r) are 0, 2.4 and 0.1 m h^{-1} respectively. Dashed lines indicate the θ surfaces. The coastline is indicated by a triangle on x-axis.

12 h (not shown) in contrast to cases C1 and C2 where they occurred at 18 h in case 1 and 15 h in C2, respectively. As time progressed (beyond 6 h), these clouds grew in height and horizontal extent. Vertical motions were much stronger (90 cm s^{-1}) for case C3 as compared to cases C1 and C2. A rainfall rate of 10 mm h^{-1} was predicted at 12 h due to stronger mesoscale convergence (not shown). The estimated mesoscale convergence at this model hour was 3.1 $\times 10^{-4}$ s^{-1} as compared to 1.5×10^{-4} and 2.3 $\times 10^{-4}$ s^{-1} for cases C1 and C2, respectively. The rainfall rate at 12 h thus increased by a factor of about 20 when the wind speed was doubled. Observations indicate the rainfall over the western Ghats to typically vary between 10 and 20 cm d^{-1} (Krishnamurti *et al.*, 1983).

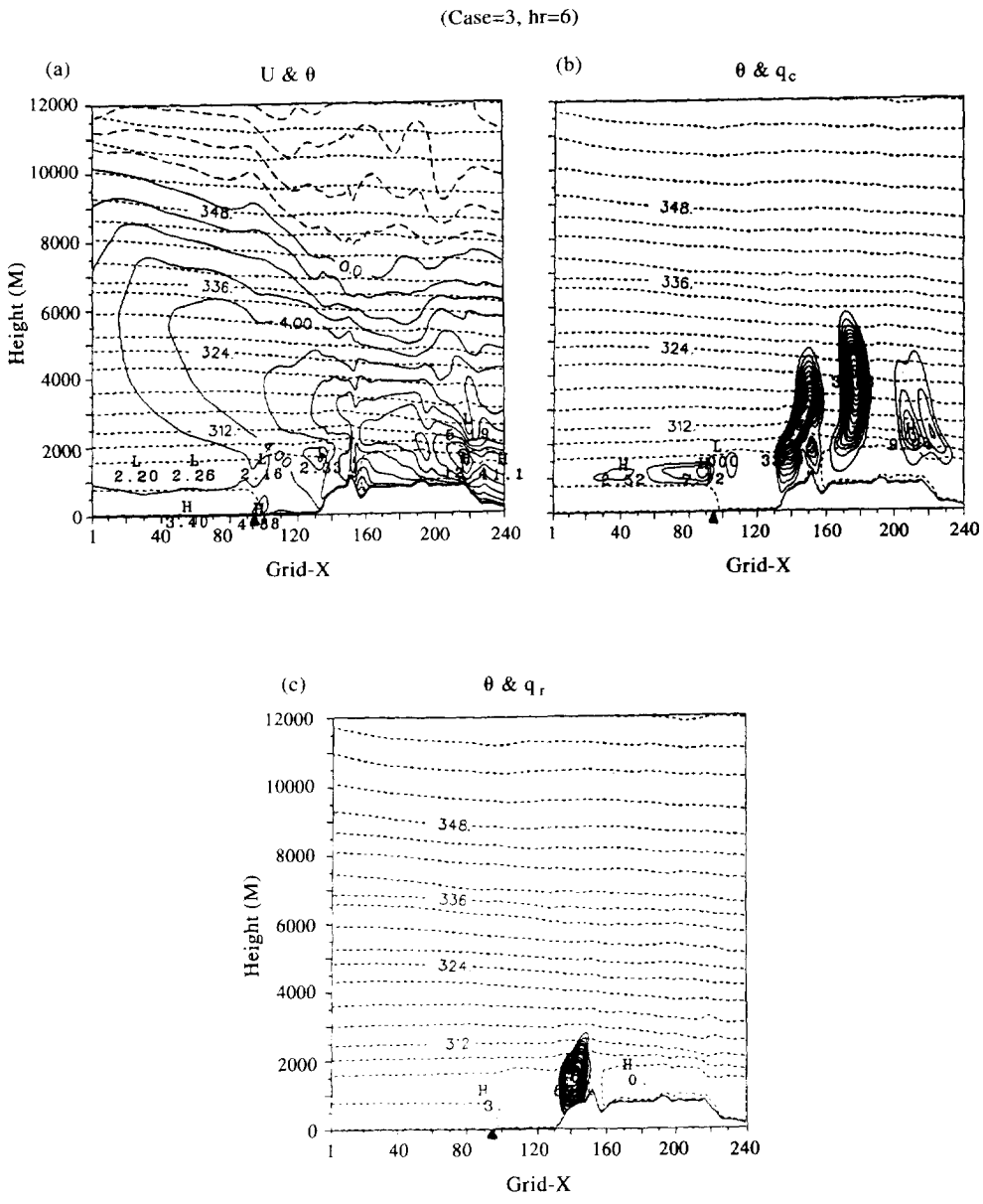

Fig. 7. Predicted (a) U and θ fields, (b) θ and cloud water, q_c (c) θ and rain water, q_r at 6 h of model simulation for Case C3. The minimum maximum and contour interval for U-field are 0, 29 and 1 m s^{-1}, respectively. The minimum, maximum and contour interval for θ-field are 297, 360 and 3 K, respectively. The minimum, maximum and contour interval for cloud water (q_c) are 0, 0.6 and 0.03 g kg^{-1}, respectively. The minimum, maximum and contour interval for rain water (q_r) are 0, 3.2 and 0.1 m h^{-1} respectively. Dashed lines indicate the θ surfaces. The coastline is indicated by a triangle on x-axis.

Distributions of cloud water and rain water at model hour 21 h (0100 LST) are shown in Fig. 8. Maximum vertical velocities decreased to 60 cm s^{-1} at 21 h from 90 cm s^{-1} at 12 h (1600 LST) of simulation. At 21 h, clouds were predicted over the coastline (Fig. 8a). Maximum cloud water over the mountains decreased slightly. Predicted rainfall rate over the mountains decreased appreciably to 5.4 mm h^{-1} (Fig. 8b) as compared to a value of 10.2 mm h^{-1} at 12 h.

In summary, increasing the ambient wind speed produced stronger mesoscale convergence and increased cloud water and rainfall rate. The effect of sea breeze circulation was to accelerate the winds near the coast and increase the vertical motion near the mountains. The land breeze was not a factor in all three

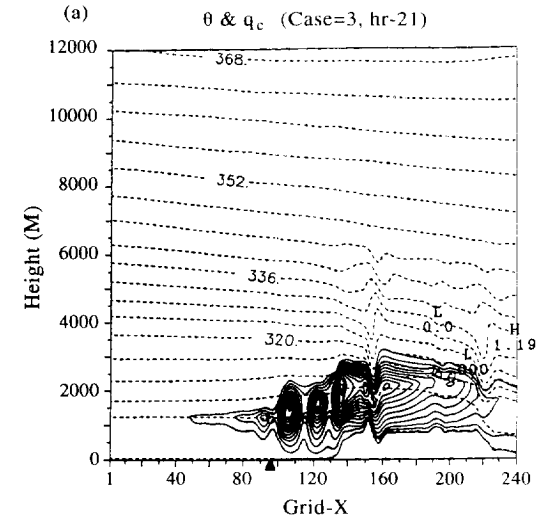

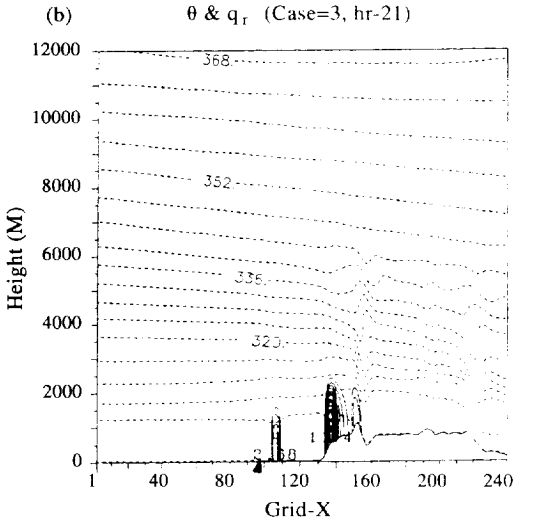

Fig. 8. Predicted (a) θ and cloud water, q_c and (b) θ and rain water q_r at 21 h of model simulation for Case C3. The minimum maximum and contour interval for θ-field are 297, 364 and 4 K, respectively. The minimum, maximum and contour interval for cloud water (q_c) are 0.72, and 0.04 g kg^{-1}, respectively. The minimum, maximum and contour interval for rain water (q_r) are 0.32, 0.2m h^{-1} respectively. Dashed lines indicate the θ surfaces. The coastline is indicated by a triangle on x-axis.

cases mainly due to small land–sea temperature differences during nighttime over the coastal region (100 km).

(b) *Without mountains.* In order to investigate the importance of orography, a numerical experiment was conducted (case C4) without the mountains. A uniform wind speed of 5 m s^{-1} was used as the initial conditions. Case C4 is same as case C2 but without the mountains. At model hour 9, convective cells formed below the boundary layer at the land–sea interface and propagated downwind (not shown). Vertical motions were also weaker without the mountains. Maximum vertical velocity was only 1.2 cm s^{-1} as compared to 35 cm s^{-1} with the mountains. No precipitation was predicted without the mountains. As time progressed, these cells weakened and slowly vanished at 15 h (1900 LST), because of the nocturnal cooling over land. Orographic lifting therefore, appears to be an important mechanism in causing precipitation over the Western Ghats.

(c) *Effect of diurnal surface heating.* Case C5 was conducted to investigate the importance of differential heating between the land and the ocean on monsoon flow. Case C5 is similar to case C3 except that the energy balance is turned off in the former case, i.e. sea–land temperature difference is maintained zero throughout the integration. A uniform wind speed of 10 m s^{-1} is used as the initial condition. The results of this case (C5) are now compared to case C3.

Figure 9 shows the distribution of cloud water and rain water after 6 and 15 h model simulation. The boundary layer is neutral over the coastal area after 6 h of integration as compared to convective conditions for case C3 at the same model hour. The cloud water distribution is similar to case C3 (Fig. 9a) over the mountains. However, in case C5, clouds do not form over the coastal area because of the absence of the sea breeze circulation. Rain water (Fig. 9b) formed downwind of the mountains as compared to upwind mountain slopes for case C3.

The thermal structure after 15 h of integration indicates a stable boundary layer over the ocean and neutral conditions over the coastal area. Distribution of cloud water in C5 is similar to C3, with a maximum value of 0.54 g kg^{-1} (Fig. 9c). For C3 with 10°C land sea temperature difference, the maximum q_c was 0.74 g kg^{-1}. However, predicted rainrate is appreciably less with only one updraft over the mountains. A rainfall rate of 1.3 mm h^{-1} (Fig. 9d) is predicted over the mountains for C5 as compared to 10.2 mm h^{-1} for C3. Increase in cloudiness and rainfall for case C3 are believed to be due to increased mesoscale convergence (3.1×10^{-4} s^{-1}) caused by the land–sea temperature difference. Precipitation in case C5 occurs only due to orographic lifting. Vertical motions are also much weaker for C5 (60 cm s^{-1}) as compared to 90 cm s^{-1} for C3. Thus sea breeze circulation appear to be an important factor in enhancing rainfall over the coast and over the mountains.

4.2. *Upwind sheared flow*

In this section, results for case C6 initialized with an observed sounding over the Arabian sea are presented. The sounding used for this case was obtained from FGGE level IIIb data (Alapaty *et al.*, 1993) and was shown in Fig. 1a. Since, low-level winds for this sounding are close to 5 m s^{-1}, model results are compared to case C2. Distributions of U, θ, q_c and q_r

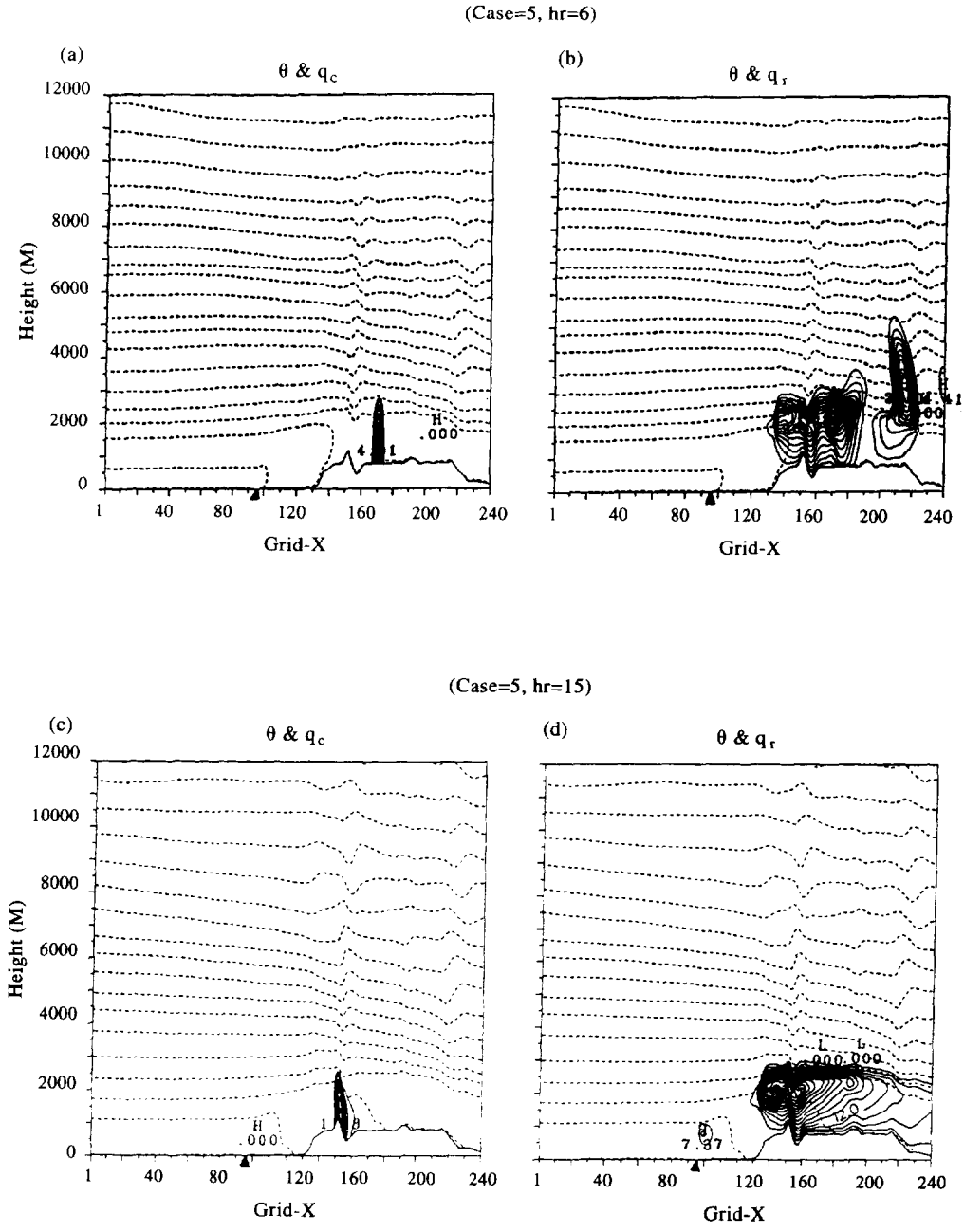

Fig. 9. Predicted (a) θ and cloud water, q_c and (b) θ and rain water, q_r after 6 h and (c) θ and cloud water and (d) θ and rain water after 15 h of model simulation for Case C5. The minimum, maximum an contour interval or θ-field at 6 h are 297, 360 and 3 K, respectively. The minimum, maximum and contour interval for cloud water (q_c) after 6 h are 0, 0.6 and 0.03 g kg^{-1}, respectively. The minimum, maximum and contour interval for rain water (q_r) are after 6 h 0.04 and 0.01 mm h^{-1} respectively. The minimum, maximum and contour interval for θ–field after 15 h are 296, 364 and 4 K, respectively. The minimum, maximum and contour interval for cloud water (q_c) after 15 h are 0.054 and 0.03 g kg^{-1} respectively. The minimum, maximum and contour interval for rain water (q_r) after 15 h are 0, 1.1 and 0.1 mm $^{-1}$, respectively. Dashed lines indicate the θ surfaces. The coastline is indicated by a triangle is on x–axis.

at model hour 6 (1000 LST) are shown in Fig. 10. Characteristics of the mountain waves, such as wave structure in the vertical and the tilting of the waves towards the upwind side are clearly seen in Fig. 10a. Distribution of the U-field is quite different compared to case C2 (uniform winds of 5 m s^{-1}). A low-level jet formed at 1500 m height with a maximum wind speed of 19.3 m s^{-1} over the coastline. Potential temperature contours (dashed lines) indicate the planetary boundary layer height to be about 2 km over the coastal

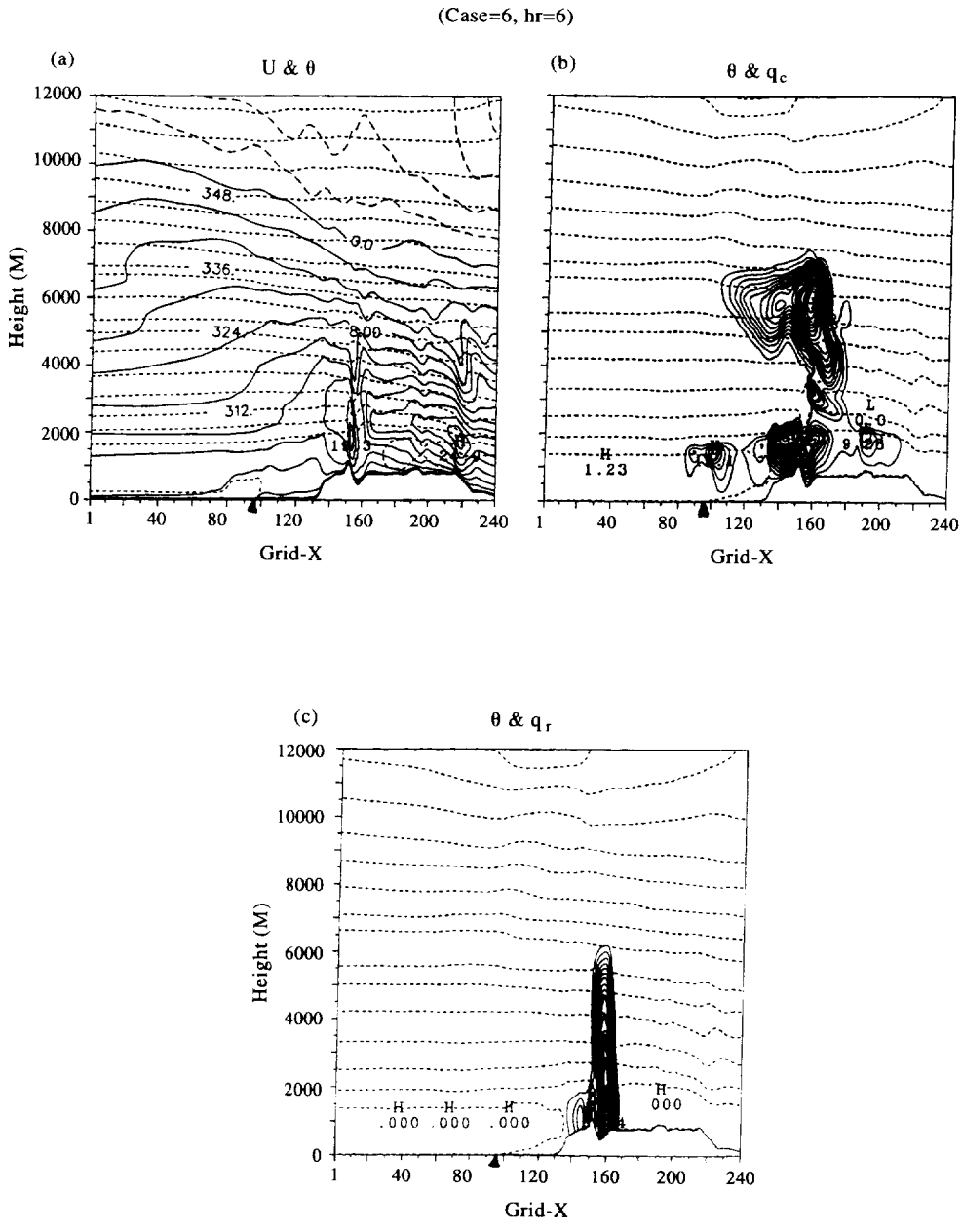

Fig. 10. Predicted (a) U and θ fields, (b) θ and cloud water, q_c (c) θ and rain water, q_r at 6 h of model simulation for Case C6. The minimum maximum and contour interval for U-field are: 9, 19 and 1 m s^{-1}, respectively. The minimum, maximum and contour interval for θ-field are 297, 360, and 4 K, respectively. The minimum, maximum and contour interval for cloud water (q_c) are 0, 0.42 and 0.02 g kg^{-1} respectively. The minimum, maximum and contour interval for rain water (q_r) are 0, 0.28 and 0.01 mm h^{-1} respectively. Dashed lines indicate the θ surfaces. The coastline is indicated by a triangle on x-axis.

area. Boundary layer thermal structure is highly convective upwind of the mountain (coastal area). Horizontal and vertical extents of cloud water (q_c) are much broader (Fig. 10b) as compared to barotropic initial conditions with uniform winds. Cumulus clouds were predicted with heights up to 8 km over the mountains. Also, broken stratocumulus clouds formed over the coast. Maximum cloud water content increased to 0.42 g kg^{-1} for sheared winds (C6) at model hour 6 as compared to 0.3 g kg^{-1} for case C2 with uniform winds. Predicted rainfall rate (Fig. 10c) has a maximum value of 0.28 mm h^{-1} over the mountains. However, no precipitation was predicted until 12 h for the case with uniform winds. Predicted maximum vertical velocity increased to 35 cm s^{-1} for this case. Maximum vertical velocity

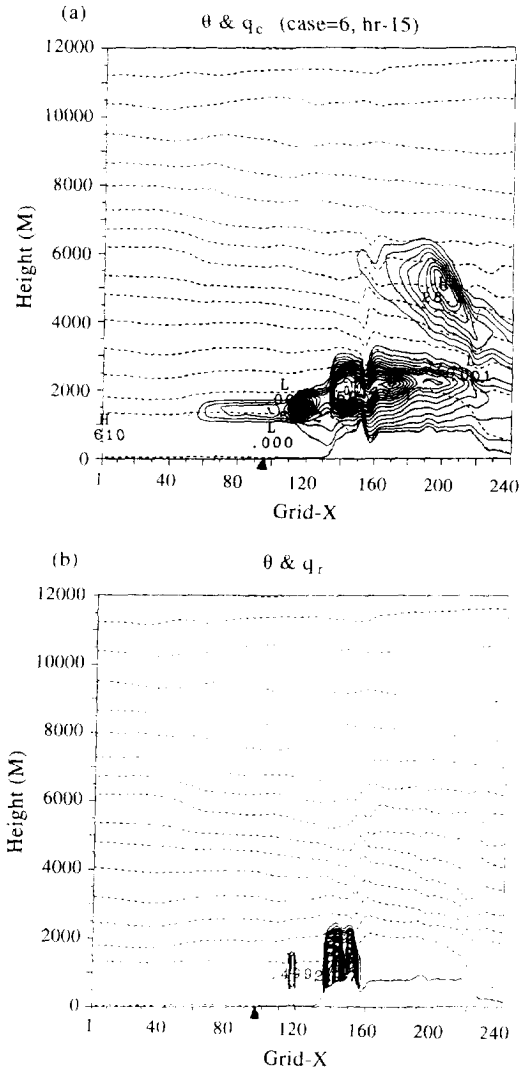

Fig. 11. Predicted (a) θ and cloud water, q_c and (b) θ and rain water, q_r at 15 h of model simulation for Case C6. The minimum maximum and contour interval for θ-field are 296, 360 and 4 K, respectively. The minimum, maximum and contour interval for cloud water (q_c) are 0, 0.57 and 0.03 g kg^{-1}, respectively. The minimum, maximum and contour interval for rain water (q_r) are 0, 2.8 and 0.1 mm h^{-1}, respectively. Dashed lines indicate the θ surfaces. The coastline is indicated by a triangle on x-axis.

was only 20 cm s^{-1} for the case with uniform winds after 6 h of integration. These differences became larger as time progressed. The model clouds intensified and advected further upwind of the mountains and even over the ocean. Rainfall occurred over the coastal area in the model simulation at 12 h of integration.

Distributions of cloud water and rain water at 15 h (1900 LST) of model simulation are shown in Fig. 11. A stable boundary layer formed at this hour over land due to nocturnal surface cooling. Clouds advected further upwind of the coastline over the ocean at this hour. A maximum cloud water of 0.6 g kg^{-1} (Fig. 11a) was predicted over the mountains and another maximum of 0.53 g kg^{-1} was predicted over the coastal area. With uniform winds (case C2), clouds were not predicted over the coastal area and over the ocean. Maximum rainfall rate (Fig. 11b) over the mountains was about 2.8 mm h^{-1} (7.5 cm d^{-1}). A rainfall rate of 0.5 mm h^{-1} was predicted over the coast. Observations indicate a typical rainfall rate of about 10–20 cm d^{-1} over the mountains (Krishnamurti *et al.*, 1983). Low-level wind shear induces stronger mesoscale convergence of 3.5×10^{-4} s^{-1} for case C6 as compared to a smaller value of 2.3×10^{-4} s^{-1} for uniform winds (Case C2) after 12 h of integration near the coast (100 km). The strong mesoscale convergence and the associated mesoscale circulations in case C6 produced larger precipitation comparable to the observations. Differences between the observations and model values could be due to the two-dimensionality of the model and lack of complete Somali jet features.

5. SUMMARY AND CONCLUSIONS

During the Indian southwest monsoon strong westerly winds occur over the Arabian sea as part of the large scale moist monsoon circulation. Because of topographic features consisting of the 1 km high Western Ghats located about 100 km inland along a fairly straight coast, orographically induced convective precipitation occurs throughout the monsoon season (June to September) along the coast and over the mountains. Maximum rainfall rates are observed to be between 10 and 20 cm d^{-1}. A two-dimensional mesoscale model with explicit cloud physics was used to isolate the effects of sea breeze/land breeze circulation and orography on monsoon rainfall. Also studied were the effects of wind speed and low-level wind shear.

The results indicate that the increase in wind speeds affect the dynamics and thermodynamics of the monsoon flow in a very consistent manner. Rainfall rate and cloud depth increased with wind speed because of increased evaporation and increased convergence. No precipitation was observed when the mountains were removed. When the land–sea temperature difference was adjusted to zero, i.e. the energy balance equation is not used over land, minimal amounts of rainfall were predicted. Sheared flow produced increased precipitation as compared to the uniform flow because of increased mesoscale convergence.

The model results did not indicate land breeze circulation during nighttime. This is because the land temperature was only 1–2°C less than the sea surface temperatures. These small horizontal gradients of surface temperature at the land–sea interface obviously could not cause perceptible land breeze circulation. Also, in the model, the relative humidity was held constant at the surface throughout the simulation period, which is a simplification. This causes moisture

flux to increase as the ground temperature increases during day time.

In summary, the two-dimensional simulations show the existence of a sea-breeze type of mesoscale circulation over the Western Ghats. This circulation enhances precipitation.

Acknowledgements—This work was supported by the Atmospheric Sciences Division of the National Science Foundation under Grant ATM-9212636 and by the Department of Energy under Contract 091575-A-Q1 with Pacific Northwest Laboratories.

REFERENCES

Alapty K., Raman S., Madala R. V. and Mohanty U. C (1993) Simulation of monsoon rainfall with Kuo and Betts Miller schemes. *J. met. atmos. Phys.* (in press).

Businger J. A., Wyngaard J. C., Izumi Y. and Bradley E. F. (1971) Flux–profile relationships in the atmospheric surface layer. *J. atmos. Sci.* **28,** 181–189.

Grossman R. L. and Durran D. R. (1984) Interaction of low-level flow with the Western Ghat mountains and offshore convection in the summer monsoon. *Mon. Wea. Rev.* **112,** 652–672.

Huang C. Y. (1990) A mesoscale planetary boundary layer model for simulations of topographically induced circulations, Ph.D. dissertation, North Carolina State University, 253 pp.

Huang C. Y. and Raman S. (1991) Numerical simulation of January 28 cold air outbreak during GALE Part I: The model and sensitivity tests of turbulence closures. *Boundary–Layer Met.* **55,** 381–407.

Huang C. Y. and Raman S. (1992) A comparative study of advection schemes with a modified WKL scheme *Mon. Wea. Rev.* **119,** 2900–2918.

Klemp J. B. and Durran D. R. (1983) An upper boundary condition permitting internal gravity wave radiation in numerical mesoscale model. *Mon. Wea. Rev.* **111,** 430–444.

Krishnamurti T. N., Cocke S., Pasch R. and Low-Nam S. (1983) Precipitation estimates from raingage and satellite observations: Summer MONEX. Dept. of Meteorology, Florida State University, 373 pp.

Mahrer Y. and Pielke R. A. (1977) The effects of topography on the sea and land breezes in a two-dimensional numerical model. *Mon. Wea. Rev.* **105,** 1151–1162.

Mellor G. L. and Yamada T. (1982) Development of a turbulence closure model for geophysical fluid problems. *Rev. Geophys. Space Phys.* **20,** 851–875.

Miller M. J. and Thorpe A. J. (1981) Radiation conditions for the lateral boundaries of limited area numerical models. *Q. J. R. Met. Soc.* **107,** 615–628.

Mukherjee A. K., Rao M. K. and Shah K. C. (1981) Vortices embedded in the trough of low pressure off Maharastra–Goa coasts during the month of July. *Indian J. Met. Hydrol Geophys.* **29,** 61–65.

Ogura Y. and Yoshizaki M. (1988) Numerical study of orographic convective precipitation over the eastern Arabian Sea and the Ghat mountains during the summer monsoon. *J. atmos. Sci.* **45,** 2097–2121.

Sarka R. P., Sinha Ray K. C. and De U. S. (1978) Dynamics of orographic rainfall. *Indian J. Met. Hydrol. Geophys.* **29,** 335–348.

Smith R. B. and Lin Y.-L. (1983) Orographic rain on the Western Ghat. In *Proc. First Sino–American Workshop on Mountain Meteorology* (edited by Reiter E. R., Baozhen Z. and Yongfu Q.), pp. 71–94.